

Global Positioning System Denied Navigation of Autonomous Parafoil Systems Using Beacon Measurements From a Single Location

Martin R. Cacan¹

Woodruff School of Mechanical Engineering,
Center for Advanced Machine Mobility,
Georgia Institute of Technology,
Atlanta, GA 30322
e-mail: martincacan@gatech.edu

Mark Costello

David S. Lewis Professor of Autonomy,
Guggenheim School of Aerospace Engineering,
Woodruff School of Mechanical Engineering,
Center for Advanced Machine Mobility,
Georgia Institute of Technology,
Atlanta, GA 30322

Edward Scheuermann

Earthly Dynamics Corporation,
Atlanta, GA 30309

Precision-guided airdrop systems have shown considerable accuracy improvements over more widely used unguided systems through high-quality position, velocity, and time feedback provided by global positioning system (GPS). These systems, like many autonomous vehicles, have become solely dependent on GPS to conduct mission operations. This necessity makes airdrop systems susceptible to GPS blackout in mountainous or urban terrain due to multipathing issues or from signal jamming in active military zones. This work overcomes loss of GPS through an analysis of guidance, navigation and control (GNC) capabilities using a single radio frequency (RF) beacon located at the target. Such a device can be deployed at the target by ground crew on site to retrieve package delivery. Two novel GNC algorithms are presented, which use either range from or direction to a RF beacon. Simulation and experimental flight testing results indicated that beacon-based methods can achieve similar results as GPS-based methods. This technology provides a simple and elegant solution to GPS blackout with best method studied showing only a 21% decrease in landing accuracy in comparison to GPS-based methods. [DOI: 10.1115/1.4037654]

1 Introduction

The accuracy of autonomously guided airdrop systems is highly dependent on the quality and richness of available feedback signals. The global positioning system (GPS) revolutionized the field of guided vehicles as it provides accurate position, velocity, and time measurements. GPS is the standard feedback signal, which provides baseline functionality of autonomous airdrop guidance, navigation and control (GNC) schemes [1–5]. Without GPS, current guided airdrop systems cannot function successfully.

While GPS is accessible nearly worldwide, conditions exist where a robust and reliable GPS signal is not guaranteed to be available. Urban and natural canyons can induce multipath propagation and satellite obscuration issues that can, respectively, degrade GPS signal quality and deny the ability of a receiver to achieve GPS lock. A greater risk lies in technology that allows adversaries to overpower the extremely low signal strength of GPS. Signal jammers can easily swamp the L1, L2, and L5 frequencies, which have received signal strengths of -157.7 dBw, -160 dBw, and -154 dBw, respectively [6].

Several vision-based systems have been implemented on various aerial platforms for navigation without GPS. Simultaneous localization and mapping is a probabilistic method in which vision information is used to construct a map of a localized environment while simultaneously tracking the position of the vehicle within the newly defined space [7]. Solved in real time using particle or extended Kalman filters, simultaneous localization and mapping methods are applicable to both two-dimensional and three-dimensional mappings and can be blended with additional onboard sensors for improved accuracy [8–10]. Many vision-based systems are used in conjunction with an inertial measurement unit to help prevent large-scale drift from single and double integration of noisy measurement data. Optical flow methods

track the apparent motion of objects (typically easily defined edges) as a camera moves through a given space [11,12]. Additionally, aerial image matching compares real-time images with a bank of preloaded satellite images of the drop zone for position estimates [13]. While these methods present viable solutions to GPS denied guided airdrop systems, they often require high quality (and heavy) camera and inertial measurement units. They are also limited to relatively low altitudes where terrain features are clearly visible and must be conducted during daylight hours on predominantly cloudless days.

Radio frequency (RF) beacons present a second classification of solutions. Commonly implemented before GPS was available, beacon technology found wide-spread use for navigation of air and sea vehicles starting with the LORAN system [14], which was developed by the U.S. during World War II. Beacon feedback enabled the first autonomous airdrop system in which scanning directional antennae identified the relative heading to the beacon and homed toward the signal source [15,16]. Additionally, beacons placed at the desired impact point (IP) can transmit signals at sufficient power to decrease their susceptibility to signal jamming. RF beacons most commonly use time of flight [17,18], but received signal strength [19], infrared detection [20], and sonar beacons [21,22] have also been utilized.

This paper aims to revitalize the application of beacon technology for use in aerial cargo delivery by conducting a study into the viability of both range to target and direction to target as a source of feedback. The inclusion of a barometric altimeter also provides altitude above ground. Experimental beacon signals are generated using GPS data to focus on the development of GNC algorithms and their capabilities.

The available signals are combined into two sets for GNC development and analysis: method 1 with $\{\psi_B, z\}$ feedback and method 2 using $\{R_B, z\}$ feedback. These two methods provide significantly less information than what is provided by GPS. As a result, vehicle position and velocity is not fully observable. One of the key challenges is the lack of atmospheric wind estimates, which are needed to actively reject their impact on the landing accuracy of the system. All guidance strategies using the feedback

¹Corresponding author.

Contributed by the Dynamic Systems Division of ASME for publication in the JOURNAL OF DYNAMIC SYSTEMS, MEASUREMENT, AND CONTROL. Manuscript received November 10, 2016; final manuscript received August 10, 2017; published online November 10, 2017. Assoc. Editor: Ming Xin.

signals above seek to land accurately while minimizing the effect of unknown atmospheric winds.

The remainder of this paper outlines and characterizes the novel GNC algorithms developed to capitalize on the available information. Section 2 provides details into each beacon-based algorithm. The simulation environment of the vehicle and atmospheric winds are presented in depth in Sec. 3, and a description of the experimental vehicle is given in Sec. 4. Discussion and results generated through extensive simulation and flight test experiments are presented in Sec. 5. Finally, a summary of the findings of this work and other conclusions are presented in Sec. 6.

2 Beacon-Based Guidance, Navigation, and Control

A schematic of a dropzone configured for beacon-guided airdrop systems is presented in Fig. 1. The beacon is assumed to be the origin of the inertial coordinate system and the desired impact point. Beacon range, R_B , is the spherical distance of the vehicle from the beacon and relative heading to beacon, ψ_B , is the angle between the vehicle's heading and horizontal position vector, r_B . Details of each guidance algorithm are presented in Secs. 2.1 and 2.2.

All methods use deflection of the trailing edge brakes as a mechanism to employ lateral control. The asymmetric control input is calculated based on the commanded turn rate and known control mapping

$$da_c = f(\dot{\psi}_c); \quad da_c \in [-1, 1] \quad (1)$$

A saturation limit of 15 deg/s is placed on the commanded turn rate to ensure excessive rocking or spiral behavior is not excited.

Finally, full symmetric brake deflection is applied just prior final impact to flare the canopy. This method is standard operating procedure as it decreases forward airspeed to soften the landing and prevent the cargo from rolling on impact.

2.1 Method 1: $\{\psi_B, z\}$ Feedback. The use of relative heading to the beacon and altitude above ground re-analyzes the initial work done in the field of guided airdrop systems [16]. Relative heading can be measured in real time using any directional antenna system such as a directional antenna or Watson-Watt antenna. This easy-to-implement feedback allows the vehicle to home toward any properly configured RF beacon.

The $\{\psi_B, z\}$ method is considered to have the most limited state observability. Both distance to target and atmospheric winds, which represent the primary metric to minimize and the greatest disturbance, respectively, are unobservable. Given limited

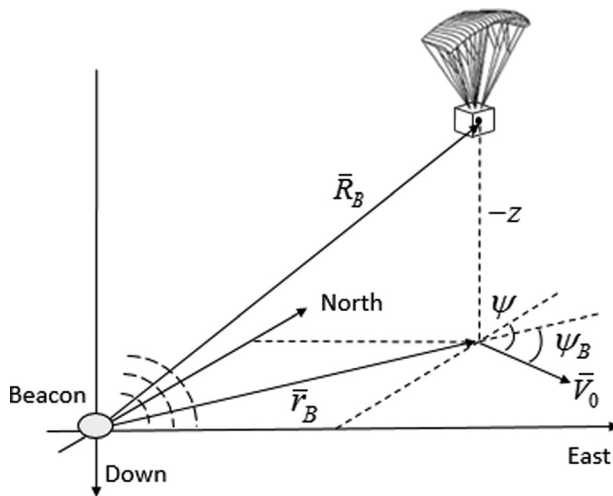


Fig. 1 Add canopy from airdrop overview figure. Try and add heading, course, velocity, beacon heading.

parameters of importance, a basic strategy of homing toward the target is implemented. The control logic always attempts to align the vehicle heading with the direction of the RF beacon. Equations (2) and (3) calculate the heading error fraction and commanded turn rate, respectively. Here, $\Delta\psi_{\max}$ is the heading error, which initiates the maximum turn rate, and $\psi_{B,\text{des}} = \pi$

$$\Delta\psi_k = \frac{\psi_{B,\text{des}} - \psi_{B,k}}{\Delta\psi_{\max}} \quad (2)$$

$$\dot{\psi}_c = \begin{cases} \dot{\psi}_{\max} & \text{for } \Delta\psi_k \geq 1 \\ -\dot{\psi}_{\max} & \text{for } \Delta\psi_k \leq -1 \\ \dot{\psi}_{\max} \Delta\psi_k \sqrt{|\Delta\psi_k|} & \text{else} \end{cases} \quad (3)$$

This controller provides excellent tracking toward the beacon when the system is far from the IP and loiters in a circular pattern near the IP for the majority of the descent. These loops are created when the vehicle reaches the IP and the heading error becomes maximum causing a 360 deg turn to re-orient toward the target. Without an estimate of the vehicle's position with respect to the target, the algorithm is unable to coordinate reaching the IP when the vehicle altitude tends to zero. As a result, the vehicle remains in the circling pattern until landing.

2.2 Method 2: $\{R_B, z\}$ Feedback. This algorithm uses measurements of spherical range from the IP and altitude above ground to steer the vehicle to the target. The use of beacon range instead of relative heading provides a direct metric to minimize improving the accuracy. This enables the vehicle to time the landing event to be when the system reaches the IP. This is conducted through a two-stage homing and loiter guidance strategy in which the vehicle attempts to either home toward or maintain a constant distance from the target. During a typical flight, the algorithm uses homing to reach the dropzone, the loiter phase to maintain proximity to the IP, and will re-enter homing to land at the target.

After deployment, the system enters homing in which the maximum inward radial velocity is tracked to reach the target. The inward velocity of the vehicle depends on the heading of the vehicle and the effects of the atmospheric winds. A bang-bang controller is used to track inward direction because a change in the vehicle's inward velocity can only be used to find the magnitude heading error, but not the sign of the error. This controller switches between maximum left and right turn rate to enforce an oscillation around the inward direction. The control effort is reversed when the radially inward acceleration goes negative indicating that the vehicle is tending away from correct heading. The controller is tuned to ensure stable tracking of the maximum inward velocity, which can vary as a result of changing atmospheric wind conditions.

When the vehicle is aligned toward the target during homing, an estimate of the radial component of the atmospheric winds is calculated by comparing the radial velocity and known vehicle airspeed. Though this estimate is subject to errors from a misalignment between vehicle heading and radial direction during the oscillatory approach, it significantly aids in the transition to the loiter period.

During the loiter period, the vehicle maintains proximity to the target by flying in a large circular trajectory with radius r_L and centered at the IP. To transition from homing to the loiter path, a 90 deg turn must be executed at the transition radius to ensure the vehicle range is close to the loiter radius at the conclusion of the turn. The transition radius is given in Eq. (4) where the final term is associated with the drift of the vehicle due to atmospheric winds

$$r_T = r_L + r_{\text{TR}} \left(1 - \frac{\pi/2}{V_0} V_{Wr} \right) \quad (4)$$

Once in loiter, a proportional-derivative (PD) controller is used to track the loiter path and reject errors induced primarily by atmospheric winds. A zero error turn rate associated with the curved path is added to the heading controller using a no-roll approximation

$$\dot{\psi}_c = \dot{\psi}_L + K_P(r - r_L) + K_D\dot{r} \quad (5)$$

$$\dot{\psi}_L = \frac{V_0}{r_L} \quad (6)$$

The effects of the atmospheric winds are minimized by the control algorithm even though they are unobservable because they directly impact the radial range and range rate of the vehicle. Similar to the previous scheme, this guidance strategy requires the vehicle to penetrate any headwinds to fully circle the desired impact point, which limits this method to atmospheric wind speeds at or below the vehicle airspeed. This is generally not a requirement for systems with full GPS feedback, which can decouple the atmospheric wind from the total vehicle motion and land accurately at the target if they are deployed sufficiently upwind of the IP.

The system re-enters homing when the current altitude is equal to the altitude required to reach the target, defined by the radial distance, airspeed, and descent rate

$$z_{\text{transition}} = r \frac{\dot{z}}{V_0} \quad (7)$$

This transition point is defined independent of the atmospheric winds making the approach to the target and overall landing accuracy heavily dependent on the low-altitude atmospheric winds.

3 Full Parafoil and Payload Simulation Environment

This section outlines the simulation model to be created to develop and validate GNC algorithms prior to experimental flight testing. This is composed of both a six degrees-of-freedom dynamic vehicle model and atmospheric wind model.

3.1 Parafoil and Payload Dynamic Model. A two-dimensional schematic of a parafoil and payload system is presented in Fig. 2. With the exception of movable parafoil brakes,

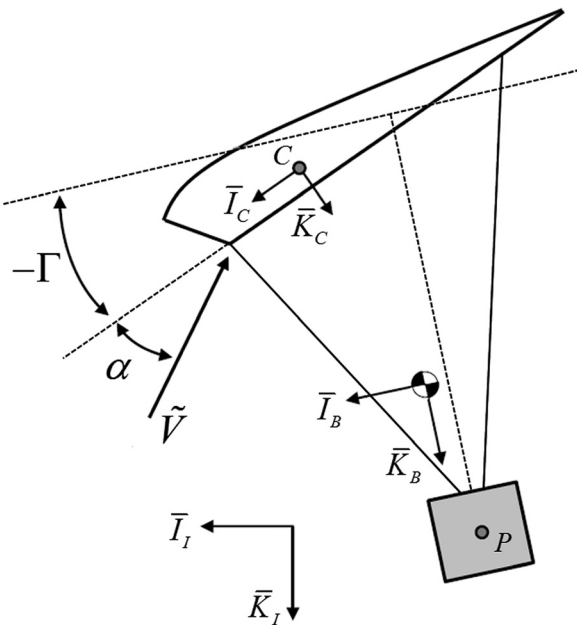


Fig. 2 Parafoil and payload schematic

the parafoil canopy is considered to be a fixed shape. The combined system of the parafoil canopy and the payload are represented by a six degrees-of-freedom, rigid-body model, defined by three inertial position components of the total system mass center as well as the three Euler orientation angles.

The transformation from inertial to body frame is conducted through a series of body-fixed 3-2-1 Euler angle rotations. This defines the kinematic relationship to calculate the body velocities and angular rates given in Eqs. (8) and (9)

$$\begin{aligned} \begin{Bmatrix} \dot{x} \\ \dot{y} \\ \dot{z} \end{Bmatrix} &= \begin{bmatrix} c_\theta c_\psi & c_\theta s_\psi & -s_\theta \\ s_\phi s_\theta c_\psi - c_\phi s_\psi & s_\phi s_\theta s_\psi + c_\phi c_\psi & s_\phi c_\theta \\ c_\phi s_\theta c_\psi + s_\phi s_\psi & c_\phi s_\theta s_\psi - s_\phi c_\psi & c_\phi c_\theta \end{bmatrix} \begin{Bmatrix} u \\ v \\ w \end{Bmatrix} \\ &= [T_{IB}] \begin{Bmatrix} u \\ v \\ w \end{Bmatrix} \end{aligned} \quad (8)$$

$$\begin{Bmatrix} \dot{\phi} \\ \dot{\theta} \\ \dot{\psi} \end{Bmatrix} = \begin{bmatrix} 1 & s_\phi t_\theta & c_\phi t_\theta \\ 0 & c_\phi & -s_\phi \\ 0 & s_\phi/c_\theta & c_\phi/c_\theta \end{bmatrix} \begin{Bmatrix} p \\ q \\ r \end{Bmatrix} \quad (9)$$

Here, $s_x \triangleq \sin(x)$, $c_x \triangleq \cos(x)$, $t_x \triangleq \tan(x)$, and $[T_{IB}]$ represent the rotation from the body to inertial reference frame.

Dynamic equations governing the translational and rotational acceleration are calculated in the body frame about the vehicle center of gravity (CG). The forces and moments considered in this work consist of gravity (W), payload aerodynamics (PA), canopy aerodynamics (CA), and apparent mass (AM). The last term is an aerodynamic phenomenon that adds additional forces and moments onto a body due to the acceleration of the fluid (air) in which a body traverses [23–25]. For systems such as parafoils that exhibit low mass and inertia compared to their volume, these effects can significantly impact the flight and turn rate dynamics. Note that forces offset from the CG are included in the total sum of the moments in Eq. (11)

$$\begin{aligned} m \left(\begin{Bmatrix} \dot{u} \\ \dot{v} \\ \dot{w} \end{Bmatrix} + \mathbb{S}_B[\bar{\omega}_{B/I}] \begin{Bmatrix} u \\ v \\ w \end{Bmatrix} \right) &= \begin{Bmatrix} X_W \\ Y_W \\ Z_W \end{Bmatrix} + \begin{Bmatrix} X_{PA} \\ Y_{PA} \\ Z_{PA} \end{Bmatrix} \\ &+ \begin{Bmatrix} X_{CA} \\ Y_{CA} \\ Z_{CA} \end{Bmatrix} + \begin{Bmatrix} X_{AM} \\ Y_{AM} \\ Z_{AM} \end{Bmatrix} \end{aligned} \quad (10)$$

$$\begin{aligned} [I_B] \begin{Bmatrix} \dot{p} \\ \dot{q} \\ \dot{r} \end{Bmatrix} + \mathbb{S}_B[\bar{\omega}_{B/I}][I_B] \begin{Bmatrix} p \\ q \\ r \end{Bmatrix} &= \mathbb{S}_B[\bar{r}_{cg \rightarrow p}] \begin{Bmatrix} X_{PA} \\ Y_{PA} \\ Z_{PA} \end{Bmatrix} \\ &+ \begin{Bmatrix} L_{CA} \\ M_{CA} \\ N_{CA} \end{Bmatrix} + \mathbb{S}_B[\bar{r}_{cg \rightarrow C}] \begin{Bmatrix} X_{CA} \\ Y_{CA} \\ Z_{CA} \end{Bmatrix} + \begin{Bmatrix} L_{AM} \\ M_{AM} \\ N_{AM} \end{Bmatrix} \\ &+ \mathbb{S}_B[\bar{r}_{cg \rightarrow C}] \begin{Bmatrix} X_{AM} \\ Y_{AM} \\ Z_{AM} \end{Bmatrix} \end{aligned} \quad (11)$$

The skew symmetric operation $\mathbb{S}_B[\bar{a}]\bar{b}$ is notation used to represent the cross product between \bar{a} and \bar{b} in the body frame by placing the measure numbers of \bar{a} in a skew symmetric matrix. The remainder of this section details how these individual forces are computed and finally, how all elements of Eqs. (10) and (11) can be combined to solve for the derivatives of body velocity and angular rate.

Gravitational forces act upon the CG of the combined parafoil and payload system, given by the below equation:

$$\begin{Bmatrix} X_W \\ Y_W \\ Z_W \end{Bmatrix} = mg \begin{Bmatrix} -s\theta \\ s_\phi c\theta \\ c_\phi c\theta \end{Bmatrix} \quad (12)$$

Aerodynamic lift and drag on the canopy is computed at point C (see Fig. 2), which represents the mean center of pressure (CP) for the canopy. The velocity of point C with respect to the atmosphere is required and transformed into the canopy frame (aligned with the airfoil) in order to calculate the aerodynamic forces

$$\begin{aligned} C_C(\vec{V}_{C/A}) &= \begin{Bmatrix} \tilde{u}_C \\ \tilde{v}_C \\ \tilde{w}_C \end{Bmatrix} \\ &= [T_{CB}] \left(\begin{Bmatrix} u \\ v \\ w \end{Bmatrix} - \mathbb{S}_B[\bar{r}_{cg \rightarrow C}] \begin{Bmatrix} p \\ q \\ r \end{Bmatrix} - [T_{BI}] \begin{Bmatrix} V_{Wx} \\ V_{Wy} \\ V_{Wz} \end{Bmatrix} \right) \end{aligned} \quad (13)$$

Based on these equations velocity, the canopy speed \tilde{V} , angle of attack α , and side slip β can be computed

$$\tilde{V} = \|\vec{V}_{C/A}\| \quad (14)$$

$$\alpha = \arctan(\tilde{w}_C, \tilde{u}_C) \quad (15)$$

$$\beta = \arcsin(\tilde{v}_C/\tilde{V}) \quad (16)$$

Provided canopy angle of attack in addition to left (δl) and right (δr) trailing edge brake deflections, the aerodynamic lift, C_L , and drag, C_D , coefficients are defined based on Eqs. (17) and (18). Here, the right-hand side parameters weight the impact of angle of attack and control inputs on the lift and drag coefficients. The individual left and right brake deflections are mapped to asymmetric (δa) and symmetric (δb) brake metrics to decouple the effect of the control surfaces into the lateral and longitudinal channels, respectively. Definition of these mappings is provided in Eqs. (19) and (20)

$$C_L = C_{L,0} + C_{L,\alpha}\alpha + C_{L,\alpha^3}\alpha^3 + C_{L,\delta b}\delta b + C_{L,\alpha\delta b}\alpha\delta b \quad (17)$$

$$C_D = C_{D,0} + C_{D,\alpha^2}\alpha^2 + C_{D,\delta b}\delta b + C_{D,\alpha\delta b}\alpha\delta b \quad (18)$$

$$\delta a = \delta r - \delta l \quad (19)$$

$$\delta b = 0.5(\delta r + \delta l) \quad (20)$$

Aerodynamic forces acting upon the CP are prescribed in Eq. (21) where lift, drag, and side forces (via $C_{Y\beta}$) are transformed from the aerodynamic frame (one aligned with the aerodynamic velocity) to the canopy frame through a single axis rotation, $[T_{CA}] \triangleq R(\bar{J}_C, \alpha)$

$$\begin{Bmatrix} X_{CA} \\ Y_{CA} \\ Z_{CA} \end{Bmatrix} = \frac{1}{2}\rho\tilde{V}^2 S_c [T_{BC}] [T_{CA}] \begin{Bmatrix} -C_D \\ C_{Y\beta}\beta \\ -C_L \end{Bmatrix} \quad (21)$$

Since all aerodynamic forces are only considered to act at the CP, the effects of a three-dimensional, dihedral wing are accounted for through canopy aerodynamic moments. These stability moments mainly provide angular rate damping to match experimental flight testing. Aerodynamic roll C_l , pitch C_m , and yaw C_n moment coefficients are defined based on the canopy angular rates and the effect of both symmetric and asymmetric brake. Equations (22)–(24) define the typical yaw-roll coupling and the impact that asymmetric brake has on the turn rate behavior of the vehicle

$$C_l = C_{l\beta}\beta + \frac{b}{2\tilde{V}}(C_{lp}\tilde{p} + C_{lr}\tilde{r}) + C_{l\delta a}\delta a \quad (22)$$

$$C_m = \frac{\bar{c}}{2\tilde{V}}C_{mq}\tilde{q} + C_{m\delta b}\delta b \quad (23)$$

$$C_n = C_{n\beta}\beta + \frac{b}{2\tilde{V}}(C_{np}\tilde{p} + C_{nr}\tilde{r}) + C_{n\delta a}\delta a + C_{n\delta a2}\delta a^2 \quad (24)$$

$$\begin{Bmatrix} L_{CA} \\ M_{CA} \\ N_{CA} \end{Bmatrix} = \frac{1}{2}\rho\tilde{V}^2 S_c [T_{BC}] \begin{Bmatrix} b C_l \\ \bar{c} C_m \\ b C_n \end{Bmatrix} \quad (25)$$

Only aerodynamic drag is considered for the payload. This calculation requires the velocity of point P to be given with respect to the atmosphere, $\vec{V}_{P/A}$, calculated identically to Eq. (13)

$$\begin{Bmatrix} X_{PA} \\ Y_{PA} \\ Z_{PA} \end{Bmatrix} = -\frac{1}{2}\rho S_p C_{D,p} \|\vec{V}_{P/A}\| \begin{Bmatrix} \tilde{u}_P \\ \tilde{v}_P \\ \tilde{w}_P \end{Bmatrix} \quad (26)$$

Finally, the apparent mass effects of the canopy are addressed. Apparent mass forces stem from the constant acceleration of displaced air in which the vehicle moves. It has been characterized that these forces have non-negligible effects on low weight to volume systems, which can significantly complicate the dynamics [23–25]. However, these references also show that the displaced fluid can be represented by manipulating the mass matrix of the vehicle. This is defined as the apparent mass $[I_{AM}] = \text{diag}(A, B, C)$ and apparent inertia $[I_{AI}] = \text{diag}(I_A, I_B, I_C)$ of the vehicle. In this work, apparent mass is considered to act on the CP of the canopy with principal axes aligned with the canopy reference frame. Apparent mass effects, defined in Eqs. (27) and (28), are based on the acceleration of the CP and angular velocity of the canopy with respect to the atmosphere. Note that atmospheric parameters are assumed to vary slowly such that their time derivatives can be neglected and the apparent mass and inertia matrices must be rotated into the body frame based on Eqs. (29) and (30)

$$\begin{Bmatrix} X_{AM} \\ Y_{AM} \\ Z_{AM} \end{Bmatrix} = -[I_{AM}]' \left(\begin{Bmatrix} \dot{u} \\ \dot{v} \\ \dot{w} \end{Bmatrix} - \mathbb{S}_B[\bar{r}_{cg \rightarrow C}] \begin{Bmatrix} \dot{p} \\ \dot{q} \\ \dot{r} \end{Bmatrix} - [T_{BI}] \begin{Bmatrix} \dot{V}_{Wx} \\ \dot{V}_{Wy} \\ \dot{V}_{Wz} \end{Bmatrix} \right) \quad (27)$$

$$\begin{Bmatrix} L_{AM} \\ M_{AM} \\ N_{AM} \end{Bmatrix} = -[I_{AI}]' \begin{Bmatrix} \dot{p} \\ \dot{q} \\ \dot{r} \end{Bmatrix} \quad (28)$$

$$[I_{AM}]' = [T_{BC}][I_{AM}][T_{BC}]^T \quad (29)$$

$$[I_{AI}]' = [T_{BC}][I_{AI}][T_{BC}]^T \quad (30)$$

By substituting the equations associated with gravity, payload aerodynamics, canopy aerodynamics, and apparent mass into Eqs. (10) and (11), the governing equation of motion is given. Note that all apparent mass effects are captured in the modified mass matrix and result in a coupling between the translational and rotational dynamics

$$\begin{bmatrix} m[I_{3 \times 3}] + [I_{AM}]' & -[I_{AM}]'\mathbb{S}_B[\bar{r}_{cg \rightarrow C}] \\ \mathbb{S}_B[\bar{r}_{cg \rightarrow C}][I_{AM}]' & [I_B] + [I_{AI}]' - \mathbb{S}_B[\bar{r}_{cg \rightarrow C}][I_{AM}]'\mathbb{S}_B[\bar{r}_{cg \rightarrow C}] \end{bmatrix} \begin{Bmatrix} \dot{u} \\ \dot{v} \\ \dot{w} \\ \dots \\ \dot{p} \\ \dot{q} \\ \dot{r} \end{Bmatrix} = \begin{Bmatrix} B_1 \\ \dots \\ B_2 \end{Bmatrix} \quad (31)$$

$$B_1 = -m\mathbb{S}_B[\bar{\omega}_{B/I}] \begin{Bmatrix} u \\ v \\ w \end{Bmatrix} + \begin{Bmatrix} X_W \\ Y_W \\ Z_W \end{Bmatrix} + \begin{Bmatrix} X_{PA} \\ Y_{PA} \\ Z_{PA} \end{Bmatrix} + \begin{Bmatrix} X_{CA} \\ Y_{CA} \\ Z_{CA} \end{Bmatrix} \quad (32)$$

$$B_2 = -\mathbb{S}_B[\bar{\omega}_{B/I}] [I_B] \begin{Bmatrix} p \\ q \\ r \end{Bmatrix} + \mathbb{S}_B[\bar{r}_{cg \rightarrow p}] \begin{Bmatrix} X_{PA} \\ Y_{PA} \\ Z_{PA} \end{Bmatrix} + \begin{Bmatrix} L_{CA} \\ M_{CA} \\ N_{CA} \end{Bmatrix} + \mathbb{S}_B[\bar{r}_{cg \rightarrow c}] \begin{Bmatrix} X_{CA} \\ Y_{CA} \\ Z_{CA} \end{Bmatrix} \quad (33)$$

3.2 Simple Shear Wind Field Model. Low-frequency, large-scale components of the wind are generated by a horizontal wind profile, which is variable between flights and constant during a particular flight. This wind field, presented in Fig. 3(a), represents low altitude wind shears by having two independent air layers with a mixing region in between. In a simple and concise manner,

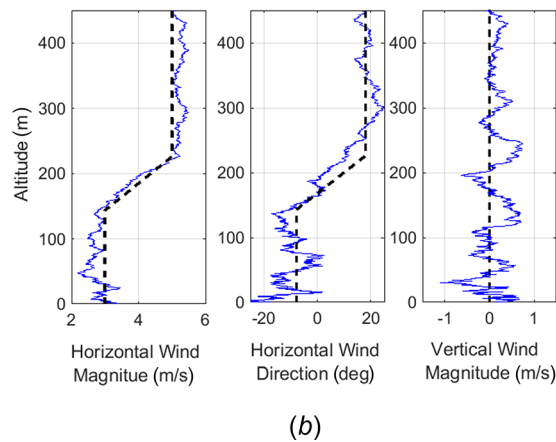
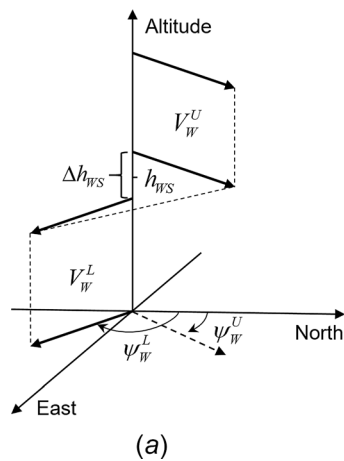


Fig. 3 (a) Horizontal wind shear model to capture large-scale spatial variations in the air mass and (b) simulated wind field, which combines base model (dashed line) with high frequency turbulence to generate total full atmospheric data (solid line)



Fig. 4 Small-scale parafoil and payload system used for experimental flight testing

this wind model captures the nature of atmospheric wind fields close to the ground, which was characterized to be a significant source of landing error by Yakimenko et al. [3]. By statistically varying air mass and mixing layer parameters, a rich variety of physical scenarios can be constructed.

To capture high frequency, small-scale components of the wind, a discrete implementation of the Dryden turbulence model was used [26,27]. Gust velocities and angular rate components are computed for all three axes by driving discrete filters with unit-variance, independent white noise signals. A sample wind field created by superimposing the simple shear model with the Dryden turbulence model is shown in Fig. 3(b). The turbulence is altitude dependent, but has the general form of high frequency, small amplitude oscillations that slowly drift around the underlying simple shear wind model.

4 Experimental Flight Vehicle

Experimental flight validation is conducted on a small-scale remote control airdrop system shown in Fig. 4. The ram air canopy has a planform area of 1.35 m² (14.5 ft²) and supports a 2.7 kg (6 lbs) payload. Extensive model parameter identification was conducted on the vehicle to tune the dynamic model

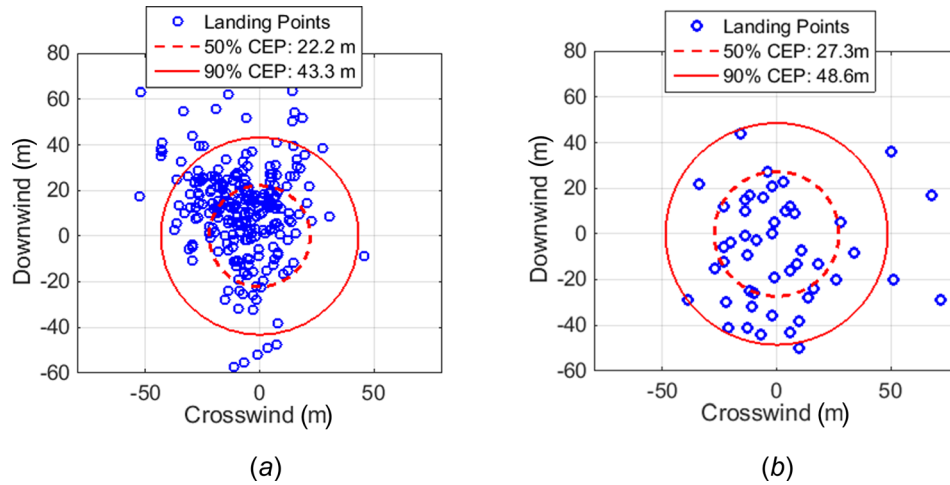


Fig. 5 Landing dispersion of GPS-based feedback algorithm in (a) simulation and (b) experimental flight testing

presented in Sec. 3. A description of the identification procedure and identified values are presented in Ref. [28], Secs. 3.2 and 3.3, respectively.

Lateral control of the aircraft is accomplished through left and right trailing edge deflection via connected servomotors. The payload is also equipped with an autopilot, electric brushless motor, speed controller, and battery. The autopilot runs the guidance, navigation, and control algorithm at 4 Hz on a PIC32MX family microcontroller and contains a sensor suite including a barometric altimeter and GPS receiver. Flight data are stored in non volatile memory and transmitted to a base station computer in real time via a 2.4 GHz XBee wireless link.

The key benefit of this system is that it can be hand launched from ground level and flown under power to gain altitude. Once at a desired release altitude, the motor is turned off and the GNC algorithm is given control of the vehicle for the descent. This simulated drop method significantly aids the development, testing, and validation of novel GNC algorithms.

5 Results

To study the capability of the proposed beacon-based algorithms, a series of simulation and experimental tests were conducted. Simulation results focused on Monte Carlo tests where parameters of the atmospheric wind model were changed between flights such that wind magnitudes varied from 0 to 6 m/s and the angle between the upper and lower air masses varied from 0 deg to 180 deg. Experimental flight testing was conducted in a large wooded clearing with gently rolling hills outside of Atlanta, GA. A release altitude of approximately 400 m was chosen to ensure there was sufficient flight time for each phase of the guidance algorithm to be executed. Similar wind conditions were ensured between all algorithms by sequentially flying each of the proposed algorithms.

In addition, a GPS-based algorithm was tested concurrently to provide a reference to more commonly accepted practices in the field of precision airdrop systems. Details of this approach are outlined in Refs. [29,30]. The Monte Carlo simulation and experimental flight test results of the GPS algorithm are presented in Fig. 5(a). Accuracy of precision airdrop systems is evaluated using the circular error probable (CEP). This metric is defined as the radius of a circle centered at the IP at which a given percentage of landings reside within. Primary accuracy is denoted by 50% CEP (equivalent to the median miss distance) and 90% CEP characterizes the extent of impacts with large miss distances. Indicated in Fig. 5 by circular lines, the GPS-based algorithm exhibited 50% and 90% CEPs in simulation of 22.2 m and 43.3 m, respectively. Misses are primarily along the downwind axis as

errors in the wind estimate cause the vehicle to undershoot and overshoot the target. Experimental results are slightly higher than those presented in simulation with 50% and 90% CEPs of 27.3 m and 48.8 m, respectively. Close alignment of results indicate agreement in the simulated and experimental flight vehicle and atmospheric winds. Note that the axes of Fig. 5 are rotated to align with the estimated wind direction calculated by the GNC algorithm such that a vehicle approaching the target into the wind would be traveling down the vertical axis.

5.1 $\{\psi_B, z\}$ Feedback. An example trajectory is presented in Fig. 6 to outline the characteristics of the $\{\psi_B, z\}$ algorithm. The vehicle is released upwind of the target following standard operating procedure and approaches the target. After, only two loops are able to align to approach the target directly into the wind. This occurs because the vehicle heading, not course direction (direction of the ground track velocity), is aligned to the target. The wind constantly perturbs the vehicle downwind of the target resulting in the approach trajectory aligning into the wind vector. When the vehicle flies over the target, the heading error becomes maximum and the vehicle makes a sharp turn to reorient toward the target. Due to unobservable winds and homing strategy of this method, the maximum wind magnitude during the flight must be less than the airspeed of the vehicle (7.2 m/s) in order for the system to penetrate any headwind. Without being able to separate vehicle velocity from atmospheric wind velocity, the system would never be

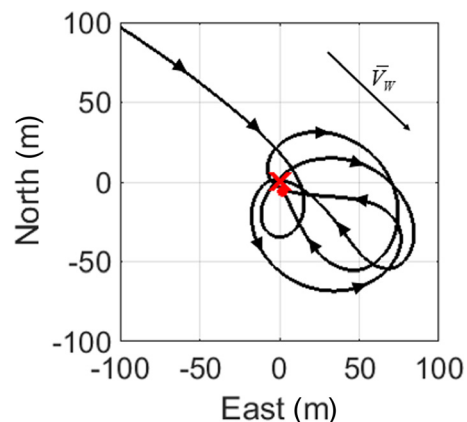


Fig. 6 Example simulated trajectory of the $\{\psi_B, z\}$ feedback algorithm

able to reach the target once it flew downwind as the strategy dictates.

This algorithm, though simple in nature, exhibits beneficial emergent behavior. As low altitude wind speeds increase, the vehicle is more prone to landing into the wind and executes a softer landing as a result of decreased ground speed. This occurs because the unobservable atmospheric wind magnitude regulates how much a given looping trajectory is stretched downwind of the target. This governs the maximum distance the vehicle gets from the IP, effectively creating an upper bound on the final miss distance. For slow atmospheric winds, the stretching behavior is not pronounced and the vehicle creates a flower pedal shaped trajectory around the IP. As atmospheric wind speed increases, the upper bound of potential miss distance also increases, but the vehicle is more likely to land facing into the wind. Intuitively, this occurs because the vehicle spends longer flying toward the target than turning to re-orient toward it. The time required to re-orient is constant (based on the 15 deg/s maximum allowed turn rate), whereas the time to fly toward the target increases as oncoming head winds slow the ground speed of the vehicle.

A Monte Carlo simulation analysis was conducted to evaluate the accuracy of this feedback method and provide quantitative justification of the emergent behavior. Results presented in Fig. 7 indicate that the vehicle lands aligned with the wind 17% of the time in low winds and 33% of the time with greater wind speeds. This metric is based on having less than a 30 deg heading error with the wind vector, which implies that a 16.6% chance of landing into the wind if the final flight direction was random.

Landing accuracy of the algorithm itself is shown in Fig. 8 with both simulation and experimental results. Simulation results

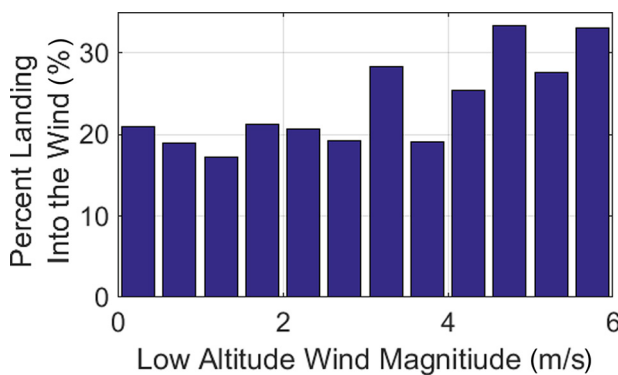


Fig. 7 Percent of landings aligned with the wind as a function of low altitude wind speeds

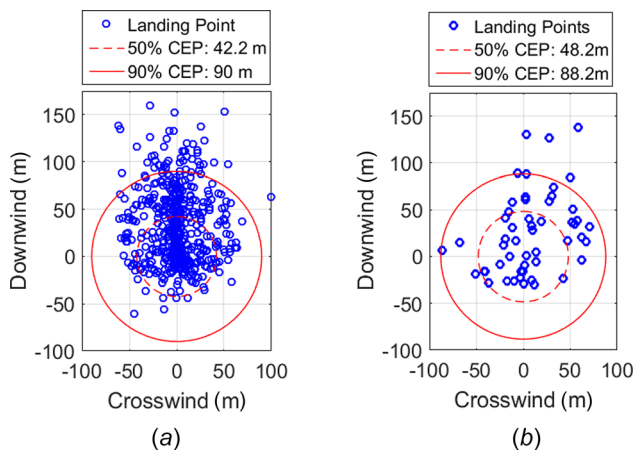


Fig. 8 Landing dispersion of the $\{\psi_B, z\}$ feedback algorithm based on (a) simulation results and (b) experimental flight testing

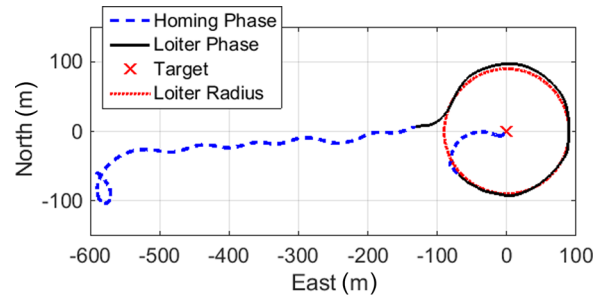


Fig. 9 Simulated trajectory of an autonomous airdrop system employing $\{R, z\}$ feedback in a windy environment

indicate that the $\{\psi_B, z\}$ feedback algorithm has 42.2 m 50% CEP and 90.0 m 90% CEP. This represents approximately a doubling in miss distance over the concurrently tested GPS algorithm with increases of 90% and 107%, respectively. Experimental results of 52 landings show similar results with 48.2 m 50% CEP and 88.2 m 90% CEP. As expected, a large number of misses occur along the downwind axis, which primarily are associated with flights that land flying toward the target. Experimental landings still tend to be downwind of the target but exhibits greater crosswind misses due to error in the heading feedback. While the high level of precision of GPS is degraded due to limited feedback, the extreme misses only slightly increase indicating that the system maintains a similar upper bound on landing accuracy.

5.2 $\{R_B, z\}$ Feedback. Using beacon range instead of beacon heading, this algorithm is able to improve accuracy by actively timing when to land at the target. An example simulated trajectory of an airdrop system employing this GNC algorithm is presented in Fig. 9. The vehicle is deployed upwind of the target following standard airdrop procedure and immediately enters initialization phase. While not actively used in this method, the initialization procedure enables a GPS-based navigation algorithm to estimate the winds for postprocessing of experimental flights. After, the system accurately homes toward the target and transitions smoothly to the loiter period. During loiter, the PD controller is able to reject the effects of the atmospheric winds by tracking the circular path. The loiter radius was selected at 90 m based on a simulated-based parameter study, which identified a trade-off between minimizing loiter radius and maximizing nominal control effort. A small loiter radius minimizes the distance the vehicle must fly during the final stage of homing, minimizing the impact of the wind on the final landing point. However, a small turn radius also increases the turn rate necessary to maintain the circular path ($\dot{\psi}_L$ in Eq. (6)) and limits the amount of control authority the PD controller has available before actuator saturation. The final homing period is able to fly toward the target but is susceptible to landing error based from the atmospheric winds. In Fig. 9, ground winds are relatively calm, which allow the system to land at the target with a miss of only 5.2 m. Note that this method also limits maximum atmospheric wind speed to be less than the vehicle velocity to ensure the system can penetrate any headwind and maintain a positive ground track velocity.

The accuracy of the $\{R, z\}$ beacon feedback method is tested in simulation through Monte Carlo analysis described earlier and experimental flight testing. Results of each analysis are presented in Fig. 10. In simulation, the $\{R, z\}$ beacon system has 50% CEP of 26.9 m and 90% CEP of 56.2 m. These results indicate only a 21% decrease in accuracy when the beacon system is used instead of GPS and a 36% improvement over the $\{\psi_B, z\}$ controller. Furthermore, large outlying miss distances are similar to the GPS system indicating that this beacon feedback method can maintain a very acceptable landing accuracy if GPS is unavailable for drop operations. 53 drops were conducted during experimental flight testing resulting in a 50% CEP landing accuracy of 22.9 m, which

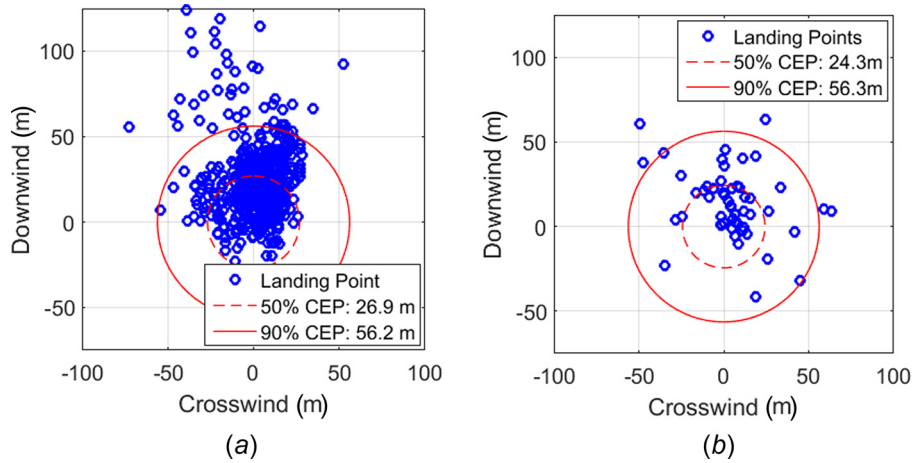


Fig. 10 Results of the $\{R, z\}$ beacon feedback method tested in (a) simulation and (b) experimental flight testing

closely matches and validates the simulation results. As noted previously, the landing accuracy of this algorithm is heavily dependent on the unobservable low altitude winds. Both simulation and experimental results in Fig. 10 show landing points, which are perturbed downwind from the IP.

6 Conclusion

This work expands the operational regime of precision airdrop systems by providing an alternative feedback method to GPS, which can be lost or actively denied. This is based on the development and analysis of guidance, navigation, and control algorithms, which use a single radio frequency beacon and onboard sensors to steer toward and land at the target. Results were generated through extensive simulation testing of a validated flight dynamic model and flight test experiments. Novel GNC algorithms used two combinations of beacon range, relative heading to beacon, and altitude above ground to expand the operating conditions of GPS denied precision airdrop systems. These methods are cheap and easy to implement, especially in comparison to vision-based systems. The proposed methods were significantly hampered by limited state observability but exhibited minimal loss in accuracy over conventional GPS-based methods. Each beacon method implemented a strategy that minimized the impact of the unknown atmospheric winds to achieve accurate landing. However, it is important to note that as a result of unobservable atmospheric winds, the application of these methods is limited to wind speeds at or below the vehicle airspeed.

Acknowledgment

The authors would like to acknowledge the support of the Natick Soldier Research Development and Engineering Center (NSRDEC) Airdrop Technology Team.

Nomenclature

$C_{D,p}$	= payload drag coefficient
$[J_B]$	= inertia matrix about the center of mass
$[I_{n \times n}]$	= identity matrix of dimension n
L, M, N	= moments exerted on the body about the body axes
m	= total vehicle mass
p, q, r	= angular velocity about the body axes
r_B	= horizontal range from beacon to airdrop system
r_T	= transition radius from homing to loiter phase
r_{TR}	= turning radius of the vehicle
R_B	= spherical distance from beacon to airdrop system

$R(\bar{I}, \gamma)$	= single axis rotation about axis \bar{I} by angle γ
S_c	= canopy surface area
S_p	= representative payload surface area
u, v, w	= velocity of the vehicle in the body frame
V_0	= vehicle airspeed
V_{Wr}	= radial component of the atmospheric winds
V_{Wx}, V_{Wy}, V_{Wz}	= inertial components of the atmospheric wind velocity
x, y, z	= inertial position of the vehicle
X, Y, Z	= forces exerted on the body along the body axes
$\delta a, \delta b$	= asymmetric/symmetric deflection of the trailing edge brakes
$\Delta\psi$	= heading error fraction
ρ	= atmospheric density
ϕ, θ, ψ	= vehicle body orientation
ψ_B	= relative heading to beacon
ψ_c	= commanded vehicle turn rate
ψ_{max}	= max allowable vehicle turn rate

References

- [1] McGrath, J., Strong, T., and Benney, R., 2005, "Status of the Development of an Autonomously Guided Precision Cargo Aerial Delivery System," *AIAA Paper No. 2005-1625*.
- [2] Benney, R., McGrath, J., McHugh, J., Meloni, A., Noetscher, G., Tavan, S., and Patel, S., 2007, "DOD JPADS Programs Overview and NATO Activities," *AIAA Paper No. 2007-2576*.
- [3] Yakimenko, O. A., Slegers, N. J., and Tladen, R. A., 2009, "Development and Testing of the Miniature Aerial Delivery System Snowflake," *AIAA Paper No. 2009-2980*.
- [4] Ward, M., 2012, "Adaptive Glide Slope Control for Parafoil and Payload Aircraft," *Ph.D. dissertation*, Georgia Institute of Technology, Atlanta, GA.
- [5] Jann, T., 2005, "Advanced Features for Autonomous Parafoil Guidance, Navigation and Control," *AIAA Paper No. 2005-1642*.
- [6] Fontana, R. D., Cheung, W., Novak, P. M., and Stansell, T., 2001, "The New L2 Civil Signal," *International GPS Conference*, Salt Lake City, UT, Sept., pp. 617–631.
- [7] Leonard, J. J., and Durrant-Whyte, H. F., 1991, "Mobile Robot Localization by Tracking Geometric Beacons," *IEEE Trans. Rob. Autom.*, **7**(3), pp. 376–382.
- [8] Kohlbrecher, S., Von Stryk, O., Meyer, J., and Klingauf, U., 2011, "A Flexible and Scalable SLAM System With Full 3D Motion Estimation," *IEEE International Symposium on Safety, Security, and Rescue Robotics (SSRR)*, Kyoto, Japan, Nov. 1–5, pp. 155–160.
- [9] Kim, J., and Sukkarieh, S., 2005, "6DoF SLAM Aided GNSS/INS Navigation in GNSS Denied and Unknown Environments," *Positioning*, **1**(9), pp. 120–128.
- [10] Kim, J., and Sukkarieh, S., 2007, "Real-Time Implementation of Airborne Inertial-SLAM," *Rob. Auton. Syst.*, **55**(1), pp. 62–71.
- [11] Ding, W., Wang, J., Han, S., Almagbile, A., Garratt, M. A., Lambert, A., and Wang, J. J., 2009, "Adding Optical Flow Into the GPS/INS Integration for UAV Navigation," *International Global Navigation Satellite Systems Society Symposium (IGNSS)*, Gold Coast, Australia, Dec. 1–3, pp. 1–13.
- [12] Giachetti, A., Campani, M., and Torre, V., 1998, "The Use of Optical Flow for Road Navigation," *IEEE Trans. Rob. Autom.*, **14**(1), pp. 34–48.
- [13] Conte, G., and Doherty, P., 2008, "An Integrated UAV Navigation System Based on Aerial Image Matching," *IEEE Aerospace Conference*, Big Sky, MT, Mar. 1–8, pp. 1–10.

- [14] Pierce, J. A., McKenzie, A., and Woodward, R. H., eds., 1948, *LORAN, Long Range Navigation*, Vol. 4, McGraw-Hill, New York.
- [15] Kane, M. T., Dicken, H., and Buehler, R., 1961, "A Homing Parachute System," Sandia Corporation, Albuquerque, NM.
- [16] Barton, W., and Knapp, C., 1968, "Controlled Recovery of Payloads at Large Glide Distances, Using the Para-Foil," *J. Aircr.*, **5**(2), pp. 112–118.
- [17] Thorbjornsen, B., White, N., Brown, A., and Reeve, J., 2010, "Radio Frequency (RF) Time-of-Flight Ranging for Wireless Sensor Networks," *Meas. Sci. Technol.*, **21**(3), p. 035202.
- [18] Lanzisera, S., Zats, D., and Pister, K. S., 2011, "Radio Frequency Time-of-Flight Distance Measurement for Low-Cost Wireless Sensor Localization," *Sens. J.*, **11**(3), pp. 837–845.
- [19] Paul, L. Y., Twigg, J. N., and Sadler, B. M., 2011, "Radio Signal Strength Tracking and Control for Robotic Networks," *Proc. SPIE*, **8031**, p. 803116.
- [20] Sultan, M. S., Chen, X., Qadeer, N., Zhang, T., and Qiang, H., 2013, "Vision Guided Path Planning System for Vehicles Using Infrared Landmark," IEEE International Conference on Robotics and Biomimetics (*ROBIO*), Shenzhen, China, Dec. 12–14, pp. 179–184.
- [21] Gadre, A. S., and Stilwell, D. J., 2005, "A Complete Solution to Underwater Navigation in the Presence of Unknown Currents Based on Range Measurements From a Single Location," IEEE/RSJ International Conference on Intelligent Robots and Systems (*IROS*), Edmonton, AB, Canada, Aug. 2–6, pp. 1420–1425.
- [22] Ferreira, B., Matos, A., and Cruz, N., 2010, "Single Beacon Navigation: Localization and Control of the MARES AUV," *MTS/IEEE OCEANS Conference*, Seattle, WA, Sept. 20–23, pp. 1–9.
- [23] Brown, G. J., 1993, "Parafoil Steady Turn Response to Control Input," *AIAA Paper No. 93-1241*.
- [24] Barrows, T. M., 2002, "Apparent Mass of Parafoils With Spanwise Camber," *J. Aircr.*, **39**(3), pp. 445–451.
- [25] Lissaman, P., and Brown, G. J., 1993, "Apparent Mass Effects on Parafoil Dynamics," *AIAA Paper No. 93-1236*.
- [26] DOD, 1990, "Flying Qualities of Piloted Aircraft," U.S. Department of Defense, Washington, DC, Report No. *MIL-STD-1797A*.
- [27] Gage, S., 2003, "Creating a Unified Graphical Wind Turbulence Model From Multiple Specifications," *AIAA Paper No. 2003-5529*.
- [28] Cacan, M. R., 2016, "Adaptive Control of Autonomous Airdrop Systems in Degraded Conditions," *Ph.D. thesis*, Georgia Institute of Technology, Atlanta, GA.
- [29] Cacan, M. R., Scheuermann, E., Ward, M., Costello, M., and Slegers, N., 2015, "Autonomous Airdrop Systems Employing Ground Wind Measurements for Improved Landing Accuracy," *IEEE/ASME Trans. Mechatronics*, **20**(6), pp. 3060–3070.
- [30] Scheuermann, E., 2015, "Autonomous Control of Parafoil and Payload Systems Using Upper Surface Canopy Spoilers," *Ph.D. thesis*, Georgia Institute of Technology, Atlanta, GA.